Materials Today Bio 32 (2025) 101680

Contents lists available at ScienceDirect

Materials Today Bio

journal homepage: www.journals.elsevier.com/materials-today-bio

Defect-engineered magnetic bismuth nanomedicine for dual-modal imaging and synergistic lung tumor therapy

Pengpeng Jia [a,b,1], Jie Tu [a,b,1], Hongyu Shen [a,b,1], Yuqin Jiang [c,1], Qiupeng Zhang [a,b], Weixian Xue [a,b], Meitong Liu [a,b], Jianbo Liu [d], Yuqing Miao [a,b], Ruizhuo Ouyang [a,b,*], Shuang Zhou [e]

[a] Institute of Bismuth and Rhenium Science, University of Shanghai for Science and Technology, Shanghai, 200093, China
[b] USST-UH International Joint Laboratory for Tumor Diagnosis and Energy Treatment, University of Shanghai for Science and Technology, Shanghai, 200093, China
[c] Collaborative Innovation Centre of Henan Province for Green Manufacturing of Fine Chemicals, Key Laboratory of Green Chemical Media and Reactions, Ministry of Education, Henan Engineering Research Centre of Chiral Hydroxyl Pharmaceutical, Henan Engineering Laboratory of Chemical Pharmaceutical and Biomedical Materials, School of Chemistry and Chemical Engineering, Henan Normal University, Xinxiang, 453007, China
[d] State Key Laboratory of Chemo/Biosensing and Chemometrics, College of Chemistry and Chemical Engineering, Hunan University, Changsha, 410082, China
[e] Cancer Institute, Tongji University School of Medicine, Shanghai, 200092, China

ARTICLE INFO

Keywords:
Fe_3O_4@Au@Bi_2S_3
NIR
Magnetic targeting
PTT
Collaborative therapy
Defect engineering

ABSTRACT

Bismuth sulfide (Bi_2S_3) nanomaterials are recognized for their potential in tumor therapy due to their narrow bandgap and low toxicity. However, limited photothermal conversion efficiency (PCE) and low carrier density restrict their broader application in photothermal cancer treatment. To address these challenges, we designed defect-engineered, magnetic-targeting Bi_2S_3-based photothermal nanoparticles, Fe_3O_4@Au@Bi_2S_3 nanorugbys (Fe_3O_4@Au@Bi_2S_3 NRs). These nanoparticles were developed using a layer-by-layer encapsulation strategy with sulfur vacancies (Vs) and Bi antisite defects (Bi replacing S, Bis), enhancing electron trapping and recombination to boost the near-infrared (NIR) response. The PCE of Fe_3O_4@Au@Bi_2S_3 NRs reached 44.34 %, which significantly improved their efficacy in photothermal treatment for lung tumors. Moreover, the polyvinylpyrrolidone (PVP) coating on the nanoparticles enabled efficient loading and pH-responsive release of doxorubicin hydrochloride (DOX), facilitating synergistic chemo-photothermal therapy. When exposed to an external magnetic field, the nanoparticles demonstrated strong magnetic targeting and enhanced computed tomography (CT) imaging capabilities, improving tumor treatment accuracy. Both in vitro and in vivo studies showed that this combined therapy effectively induced cancer cell apoptosis and inhibited tumor proliferation, showcasing outstanding anti-tumor performance. This study provides a promising strategy for enhancing chemo-photothermal therapy through defect-engineered, magnetic-targeted Fe_3O_4@Au@Bi_2S_3 nanoparticles, holding significant potential for clinical applications in tumor therapy.

1. Introduction

Lung cancer accounts for approximately 11.4 % of all cancer cases and is the leading cause of cancer-related deaths globally, making it the most commonly diagnosed cancer type worldwide [1]. In recent years, non-invasive treatments that activate nanomaterials through external stimuli have emerged as revolutionary approaches for effective lung cancer therapy. These nanomaterial-based methods significantly enhance treatment efficacy by leveraging the unique properties of nanomaterials [2]. Photothermal therapy (PTT), which uses near-infrared (NIR) light to activate nano-photothermal agents that convert light energy into heat, has shown great potential for clinical tumor treatment due to its non-invasive nature, high specificity, and precise spatial-temporal control [3,4]. Among various nanomaterials, narrow bandgap bismuth sulfide (Bi_2S_3) nanomaterials have gained prominence in tumor PTT for their favorable photothermal absorption properties and low toxicity [5–7]. However, the low carrier density of Bi_2S_3 limits its photothermal conversion efficiency (PCE, η), restricting

* Corresponding author. Institute of Bismuth and Rhenium Science, University of Shanghai for Science and Technology, Shanghai, 200093, China.
E-mail address: ouyangrz@usst.edu.cn (R. Ouyang).
[1] P. Jia, J. Tu, H. Shen, and Y. Jiang contributed equally to this work.

https://doi.org/10.1016/j.mtbio.2025.101680
Received 23 November 2024; Received in revised form 28 February 2025; Accepted 17 March 2025
Available online 18 March 2025

its broader therapeutic application. Notably, introducing defects in Bi_2S_3 can significantly enhance its photothermal properties by improving the photothermal conversion mechanism [8]. Despite this, few studies have explored defect engineering in Bi_2S_3 for PTT, thereby limiting the advancement of its PCE. A promising approach is to integrate tumor-targeted, multifunctional nanosystems through defect engineering, combining diagnosis and therapy for improved outcomes.

To achieve specific cancer diagnosis and treatment using Bi_2S_3-based nanomaterials, it is essential to construct a theranostic nanoplatform that integrates tumor targeting, drug delivery, photothermal properties, and bioimaging. Iron oxide nanoparticles (Fe_3O_4, Fe_2O_3 NPs) are widely used in preclinical and clinical applications as contrast agents for magnetic resonance imaging (MRI) and drug carriers for targeted drug delivery [9,10]. These nanoparticles exhibit excellent magnetic properties and high-resolution MRI capabilities, making them ideal for magnetic targeting of specific pathological sites under an external magnetic field [11,12]. Unlike molecular-targeted therapies, magnetic targeting does not rely on the expression of specific receptors [13]. Compared with other photothermal agents, Fe_3O_4 nanospheres (NSs) have broad red/-NIR wavelength absorption, showing excellent photothermal properties. The unique magnetic targeted aggregation not only causes a redshift in the visible-NIR spectrum, which affects their heating ability when irradiated with NIR [14], but also increases their NIR laser absorption and produces a stronger tumor photothermal clearance effect in vivo [15]. Once Fe_3O_4 NSs accumulate in the tumor microenvironment (TME), they release heat through a 'magnetic hysteresis effect' under an alternating magnetic field and generate additional heat via photothermal effects in the NIR region [16,17]. When the local temperature rises to 43–48 °C, tumor cell apoptosis can be triggered. Fe_3O_4 NSs also contribute to cancer immunotherapy by promoting macrophage polarization into pro-inflammatory M1 phenotypes, thereby enhancing immune responses and preventing liver metastasis [18]. In recent work, Au-Fe_3O_4 Janus nanoparticles were developed for tumor imaging, and these nanoparticles induced targeted PTT via magnetic targeting and T-weighted MRI [19]. Importantly, nanoparticle geometry plays a critical role in PCE, with symmetrical nanostructures demonstrating strong absorption resonance [20]. The core-shell structure, with Fe_3O_4 as the core, offers high homogeneity and symmetry, facilitating stronger photothermal absorption and preventing premature deactivation of Fe_3O_4 [21].

Bi_2S_3 nanomaterials, as narrow-bandgap semiconductors, exhibit excellent NIR absorption properties, making them suitable for NIR-triggered PTT [22]. Upon photon excitation, semiconductors generate electron-hole (e^--h^+) pairs, and the resulting excited electrons release energy via radiative (photon emission) or non-radiative (phonon emission) relaxation [20]. Non-radiative relaxation is particularly relevant for PTT, as it transfers energy to the material's lattice, increasing lattice temperature and enabling the conversion of light to heat [23,24]. Two primary mechanisms—Shockley-Read-Hall recombination and Auger recombination—govern this process [25]. Auger recombination, which is e^--h^+ recombination, depends on the bandgap and bandgap energy, while Shockley-Read-Hall recombination is defect-assisted and occurs through mid-gap energy states (trap levels) created by material defects [26]. These traps facilitate electron capture from the conduction band (CB), leading to recombination with valence band (VB) holes and the generation of phonons, thus releasing thermal energy [27]. Therefore, defect engineering is an effective strategy for improving the PCE of semiconductors by enhancing e^--h^+ recombination and extending electron participation in catalytic reactions [28]. Given the narrow bandgap and low carrier density of Bi_2S_3, defect construction can enhance electron trapping, promoting Shockley-Read-Hall recombination and boosting phonon-driven photothermal conversion.

Previous studies have shown that sulfur vacancies (Vs) and bismuth antisite defects (Bi replacing S, Bis) can be easily generated in Bi_2S_3 under bismuth-rich and sulfur-deficient conditions, reducing defect formation energy [29]. Moreover, noble metals like Au, which bind closely to sulfur (S) atoms in Bi_2S_3, can increase S atom loss and introduce Vs in the Bi_2S_3 lattice, where enriched bismuth (Bi) atoms take the place of S atoms, resulting in more Bis defects [30,31]. Layered Au and Bi_2S_3 nanoshells can significantly increase the number of defects in Bi_2S_3. Additionally, Au nanomaterials have excellent biocompatibility, high NIR absorption, and superior PCE, making them ideal candidates for cancer PTT [32]. The combination of Au and Bi_2S_3 compensates for the low carrier density of Bi_2S_3, with Au generating strong localized surface plasmon resonance (LSPR) that enhances photothermal conversion through electron-phonon scattering [33]. In previous work, we developed Au@Bi_2S_3 nanobones, which demonstrated enhanced photothermal properties and NIR-triggered PTT [5]. However, Bi_2S_3's poor solubility necessitates surface modification for biological applications. Polyvinyl pyrrolidone (PVP), a water-soluble polymer, can improve the solubility and biocompatibility of hydrophobic nanomaterials while enabling pH-responsive drug delivery [34,35]. In chemical photothermal therapy, the novel polymetallic sulfide-doped mesoporous silica nanomaterial developed by Zhang et al. exhibits not only effective photothermal therapeutic properties but also excellent doxorubicin (DOX) loading efficiency due to its unique hollow and mesoporous structures [36]. However, DOX inevitably suffers losses during in vivo delivery. Yang et al. co-loaded DOX and copper sulfide (CuS) nanoparticles in $CaCO_3$ and functionalized the PEG surface to achieve efficient DOX delivery and controlled release in response to pH and NIR laser stimuli, but the DOX loading was limited to 2.53 % [37]. Notably, the strong electrostatic interactions between PVP and DOX facilitate efficient loading and delivery, enabling control under pH and NIR laser responses, thereby significantly enhancing the efficacy of chemical photothermal therapy [38,39].

In this study, we designed and synthesized multifunctional magnetic Fe_3O_4@Au@Bi_2S_3 nanorugbys (NRs) with sulfur vacancies for chemo-photothermal therapy and computed tomography (CT) imaging guidance. Fe_3O_4 NSs served as the magnetic core, while Au and Bi_2S_3 layers were applied via hydrothermal reduction. PVP was used to modify the surface for improved biocompatibility, and DOX was loaded for synergistic chemo-photothermal therapy. Under 808 nm NIR laser irradiation, the Fe_3O_4@Au@Bi_2S_3 NRs exhibited enhanced photothermal conversion (η = 44.34 %) due to LSPR-induced phonon generation and non-radiative relaxation. The magnetic core enabled targeted drug delivery and enhanced CT imaging. Both in vitro and in vivo studies confirmed the potent anti-tumor effects of Fe_3O_4@Au@Bi_2S_3/PVP-DOX NRs, demonstrating their potential for magnetically targeted chemo-photothermal therapy (Scheme 1).

2. Results and discussion

2.1. Characterizations of Fe_3O_4@Au@Bi_2S_3/PVP NRs

The Fe_3O_4@Au@Bi_2S_3/PVP NRs were synthesized via a layer-by-layer modification method, as illustrated in Scheme 1 [40–43]. Initially, Fe_3O_4 nanospheres (NSs) were synthesized by coprecipitating iron (III) chloride hexahydrate ($FeCl_3{\cdot}6H_2O$) and iron (II) chloride tetrahydrate ($FeCl_2{\cdot}4H_2O$). Transmission electron microscopy (TEM) images revealed that the resulting Fe_3O_4 NSs exhibited a uniform spherical morphology with an approximate diameter of 10.9 nm, although slight agglomeration was observed (Figs. S1a–c). Subsequently, the Au nanoshell was thermally reduced from chloroauric acid ($HAuCl_4$), coating the magnetic Fe_3O_4 core to form Fe_3O_4@Au nanoparticles (NPs) without significantly altering their spherical shape. The diameter of the nanoparticles increased to 27–30 nm, as shown in Figs. S1d–e. The threefold increase in particle size can be attributed to the following reasons: First, the concentration of sodium citrate influenced the pH of the reaction system, significantly reducing the negative ζ-potential of Au nanocrystals in the citrate solution [44]. This weakened the repulsive interactions between nanocrystals caused by their negative charges, promoting aggregation. Second, Fe_3O_4 NSs are prone to aggregation due

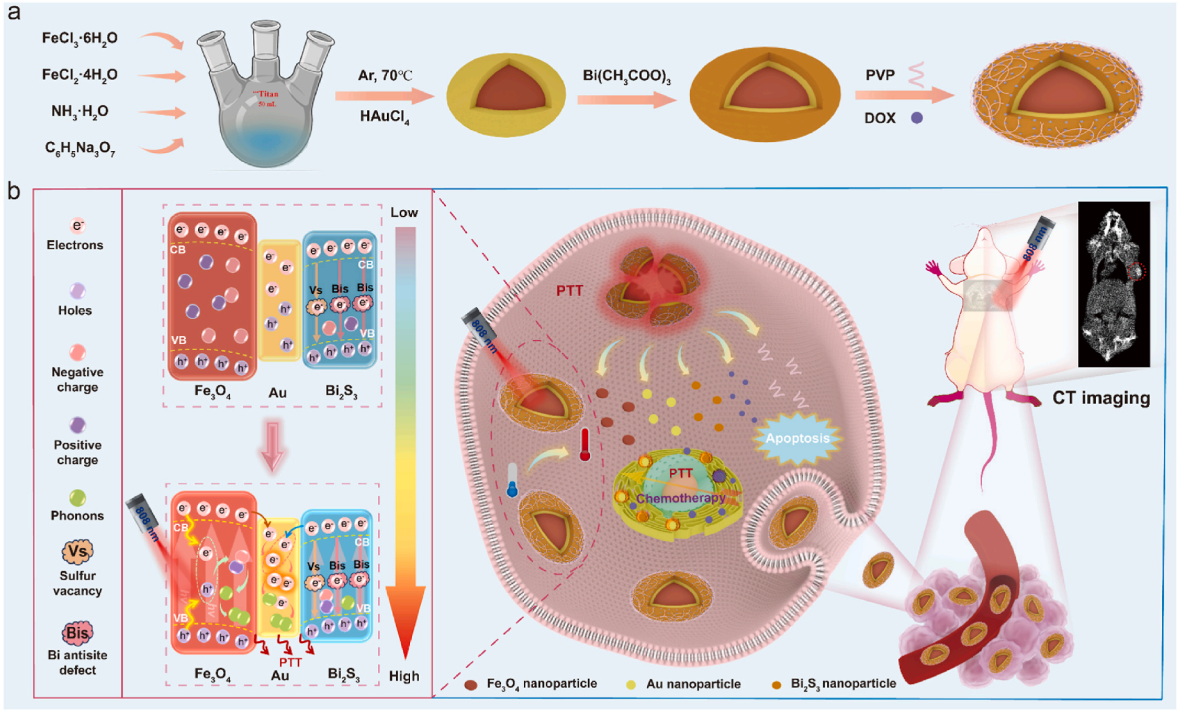

Scheme 1. Schematic illustration of the synthesis process and multimodal synergistic antitumor therapy mechanism of Fe_3O_4@Au@Bi_2S_3/PVP-DOX NRs. The synthesis involves a layer-by-layer construction of Fe_3O_4 core, Au, and Bi_2S_3 shells, followed by surface modification with PVP and drug loading with DOX. The resulting multifunctional nanorugbys enable precise targeting under an external magnetic field, combined with photothermal ablation and controlled drug release, offering a synergistic approach to cancer therapy.

to strong magnetic interactions, and a small number of Au nanoshells may encapsulate more than one iron oxide nanoparticle.

With the assistance of hexadecyl trimethyl ammonium bromide (CTAB), the outer Bi_2S_3 shell was generated in a bismuth-rich and sulfur-deficient environment, producing ellipsoidal Fe_3O_4@Au@Bi_2S_3 nanorugbys (NRs). The sulfide ions selectively facilitated the growth of the Au shell by quenching or reducing the Au precursor, and adsorbing onto the surface of the Au nanorods [42,45]. The crystalline growth direction was further regulated by the presence of external ions, in the presence of the sulfur source thioacetamide (TAA) and CTAB-modified Fe_3O_4@Au NPs, the morphology of the nanocomposites transformed from spherical to ellipsoidal during Bi_2S_3 shell formation. The TEM image in Fig. 1a shows that the transverse diameter of the as-prepared Fe_3O_4@Au@Bi_2S_3 NRs increased to 44 ± 2 nm, while the longitudinal diameter extended to 32 ± 2 nm. Dynamic light scattering (DLS) analysis indicates that Fe_3O_4@Au@Bi_2S_3 NRs have an average particle size of 146 nm (Fig. S2a). We speculate that the observed increase in particle size may be attributed to magnetic adsorption. The HR-TEM image reveals distinct lattice spacings of 0.25 nm and 0.27 nm, corresponding to the (240) and (211) planes of Bi_2S_3, respectively (Fig. S1f) [46]. This confirms the successful modification of Bi_2S_3 on the surface of Fe_3O_4@Au@Bi_2S_3 NRs. We further conducted energy-dispersive X-ray spectroscopy (EDS) element mapping (Fig. 1c–h) and line-profile elemental mapping analysis (Fig. 1j), revealing the multi-element composition and uniform horizontal distribution of Fe_3O_4@Au@Bi_2S_3 NRs. Additionally, the surface modification with PVP did not significantly alter the rugby-like shape of the Fe_3O_4@Au@Bi_2S_3 NRs (Fig. 1b).

The ultraviolet–visible (UV–vis) absorption spectra tracked the entire synthesis process of Fe_3O_4@Au@Bi_2S_3 NRs. As shown in Fig. 1i, Fe_3O_4 NSs exhibited a decreasing absorption curve (pink line 1) with no distinct absorption peak. After forming around the Fe_3O_4 NSs, a characteristic absorption peak appeared at 560 nm for Fe_3O_4@Au NPs (orange line 2), indicating the successful formation of the Au shell. A red shift in this peak occurred after the Bi_2S_3 nanolayer was added (blue line 3), confirming the successful fabrication of Fe_3O_4@Au@Bi_2S_3 NRs [41,43]. Moreover, a slight enhancement in near-infrared (NIR) absorption intensity between 800 and 900 nm was observed after Bi_2S_3 was incorporated, suggesting successful defect engineering that increased electron trapping and facilitated charge carrier recombination. The color change of the material throughout the layer-by-layer coating process also corresponded with the increase in NIR absorption, and the final deepened color confirmed the successful Bi_2S_3 coating and improved photothermal performance (Fig. 1i).

The magnetic properties of the Fe_3O_4@Au@Bi_2S_3 NRs were demonstrated in Fig. S2b, where the nanoparticles dispersed in water were magnetically attracted to the side of the vial within 5 min when subjected to an external magnetic field. Further analysis of the magnetic properties at room temperature (Fig. 1k) revealed a typical hysteresis loop, confirming the superparamagnetic nature of the Fe_3O_4@Au@Bi_2S_3 NRs under an external magnetic field of 10,000 Oe. The magnetization of the Fe_3O_4@Au@Bi_2S_3 NRs was 37.11 emu/g, sufficient for magnetic targeting applications, and exceeded values reported for similar nanomaterials (Table S1).

X-ray photoelectron spectroscopy (XPS) was used to analyze the elemental composition and chemical states of the synthesized Fe_3O_4@Au@Bi_2S_3 NRs. The XPS survey spectrum (Fig. 2a) confirmed the presence of all expected elements in the Fe_3O_4@Au@Bi_2S_3 NRs. The C 1s peak at a binding energy of 284.50 eV increased significantly after PVP modification, attributed to the C–C chains of both PVP and residual CTAB. The appearance of the C 1s peak at 288.50 eV was assigned to the carbonyl group in PVP. The Fe 2p spectrum showed two distinct peaks at 723.50 eV and 710.40 eV, corresponding to Fe $2p_{1/2}$ and Fe $2p_{3/2}$, respectively, primarily due to Fe_3O_4 and partial oxidation to Fe_2O_3 (Fig. 2b). The O 1s spectrum displayed three peaks at 533.30 eV, 531.95 eV, and 529.70 eV, which were likely due to residual water, Fe_2O_3, and Fe_3O_4, respectively (Fig. 2c). In the Au 4f spectrum (Fig. 2d), the peaks for Au $4f_{5/2}$ and Au $4f_{7/2}$ were observed at 87.38 eV and 83.70 eV, respectively, showing a slight shift (~0.48 eV) compared to Au NPs [47]

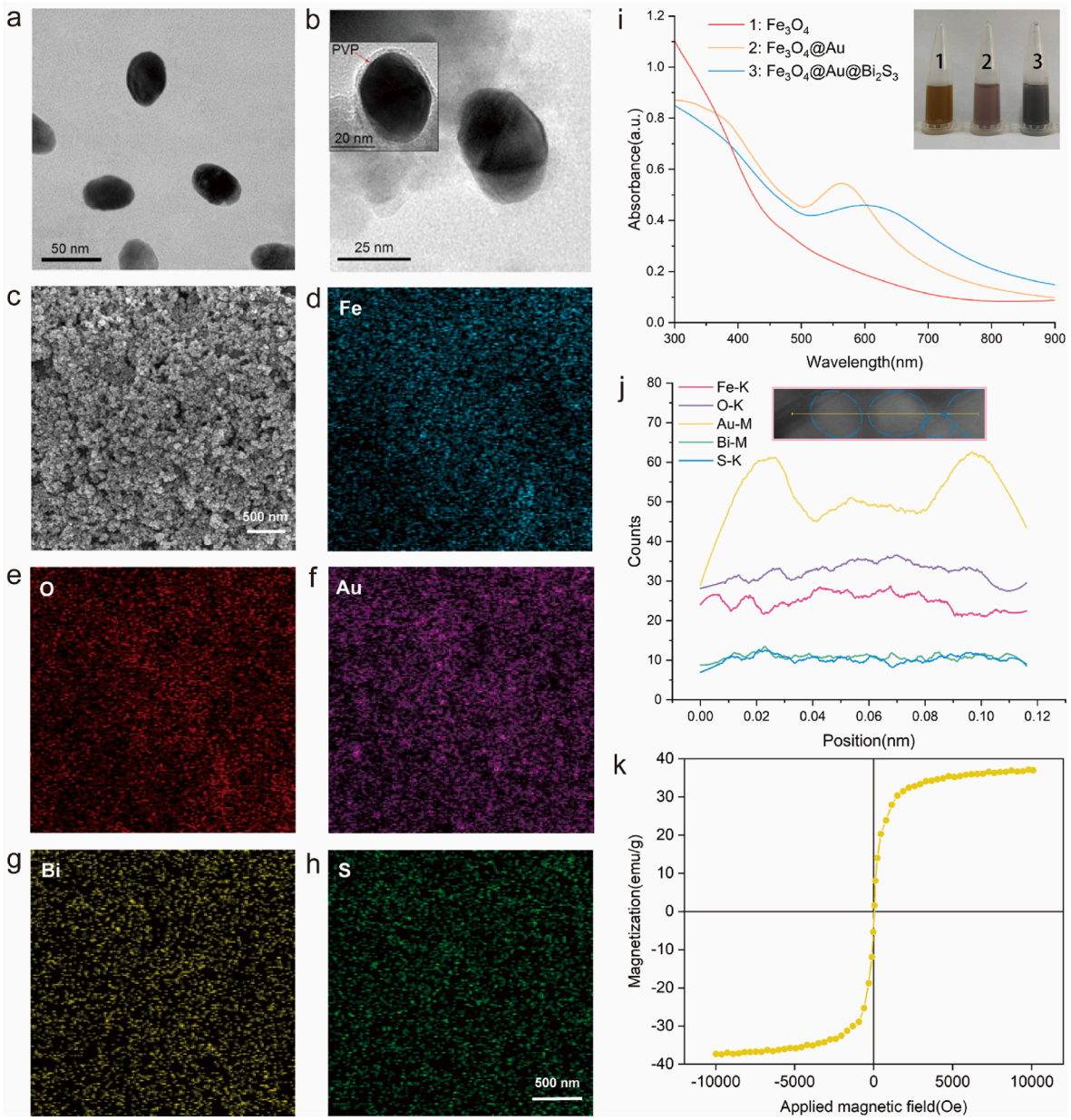

Fig. 1. TEM images of (a) Fe_3O_4@Au@Bi_2S_3 and (b) Fe_3O_4@Au@Bi_2S_3/PVP NRs; (c) SEM image and (d–h) elemental mapping of Fe_3O_4@Au@Bi_2S_3 NRs; (i) UV–vis absorption spectra of (1) Fe_3O_4 NSs, (2) Fe_3O_4@Au NPs, and (3) Fe_3O_4@Au@Bi_2S_3 NRs; (j) Scanning position and EDS spectrum of Fe_3O_4@Au@Bi_2S_3 NRs; (k) Magnetization loop of Fe_3O_4@Au@Bi_2S_3 NRs.

and Fe_3O_4@Au NPs [48]. This shift was attributed to the formation of Au-S bonds upon the binding of Au to the Bi_2S_3 nanoshells (Fig. 2g), contributing to the formation of Bis defects [49]. The Bi 4f peaks were observed at 164.00 eV and 159.50 eV for Bi $4f_{5/2}$ and Bi $4f_{7/2}$, respectively (Fig. 2e), slightly higher than typical Bi 4f binding energies (~1.50 eV) [50]. The increased binding energy was likely caused by the close binding between Bi_2S_3 and Au, resulting in the formation of Bis defects due to the higher Pauling electronegativity of Au (2.54) compared to Fe (1.80) and Bi (2.02), leading to electron transfer [31,51]. The S 2p spectrum (Fig. 2f) revealed peaks at 164.00 eV and 158.88 eV, corresponding to S $2p_{3/2}$ and S $2p_{1/2}$, respectively, which aligned with the binding energy of S^{2-}. The peak at 164.00 eV also suggested the presence of Au-S bonds [52]. These XPS results confirm the successful synthesis of Fe_3O_4@Au@Bi_2S_3/PVP nanocomposites and the effective introduction of sulfur vacancies.

Fig. 2g comprehensively elucidates the photothermal conversion mechanism of Fe_3O_4@Au@Bi_2S_3 NRs: Upon photon absorption, Fe_3O_4 facilitates electron transition, generating e^--h^+ pairs. During recombination, these carriers collide with adjacent ones, releasing energy through phonon-phonon scattering, which is ultimately converted into thermal energy [26]. Following energy absorption by Au, non-radiative plasmon decay generates hot electrons that undergo rapid collisions with low-energy electrons, converting their energy into thermal energy. This energy is subsequently transferred to the lattice through electron-phonon interactions, followed by thermal dissipation to the surrounding environment via phonon-phonon scattering [20]. The strong Au-S bonding in Bi_2S_3 induces the formation of Vs and Bis defects, which create intermediate gap states capable of electron trapping. These trapped electrons subsequently transition from the CB to the VB via defect levels, where they recombine with holes. The resulting phonons interact with the lattice, facilitating efficient thermal energy transfer [20,25,27]. Furthermore, the crystal defect-accelerated dephasing of the plasmon generates significant non-radiative damping, promoting increased energy absorption by hot electrons and subsequent conversion

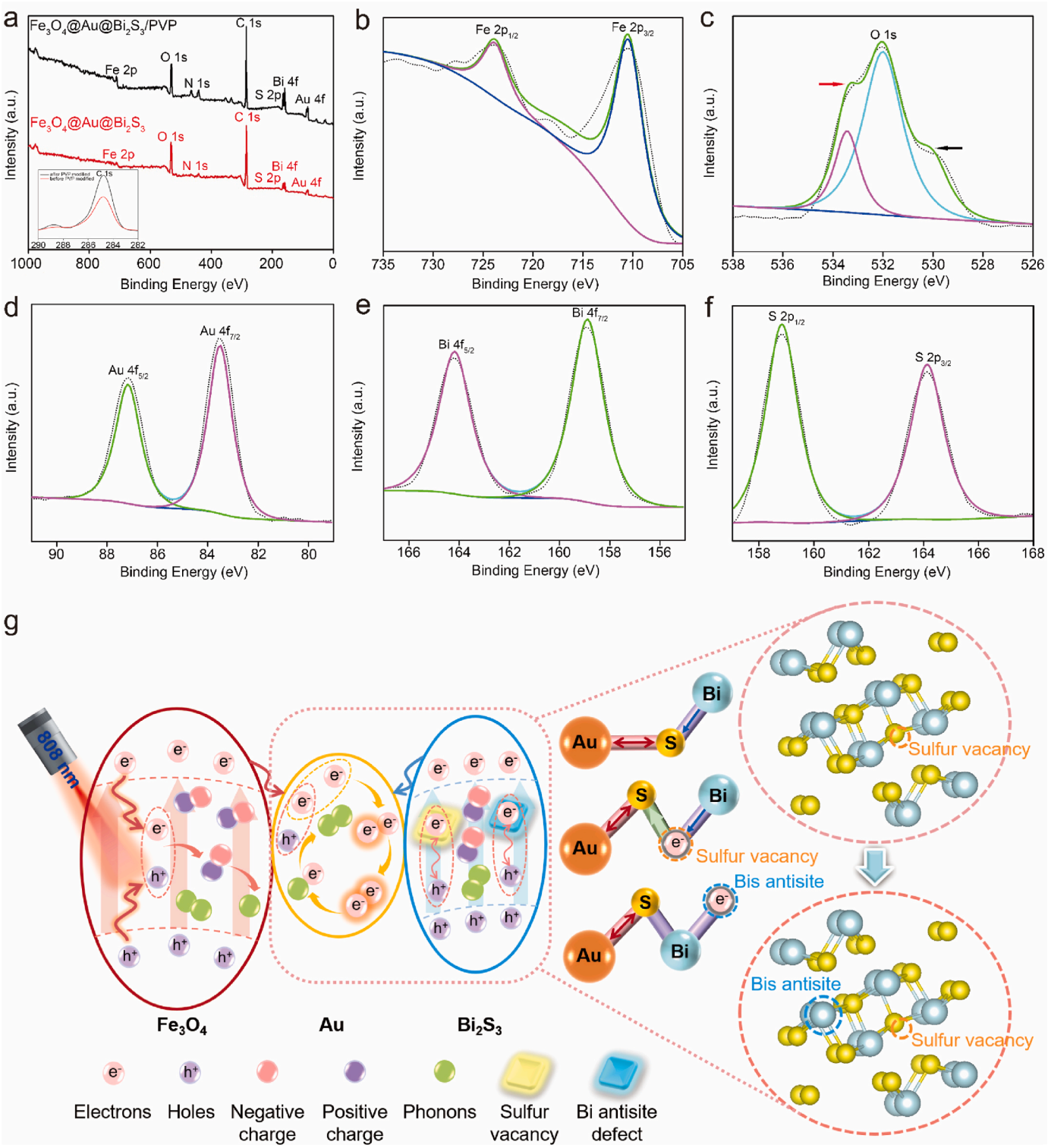

Fig. 2. (a) XPS survey spectra of Fe_3O_4@Au@Bi_2S_3 NRs and Fe_3O_4@Au@Bi_2S_3/PVP NRs; Fitted spectra of (b) Fe 2p, (c) O 1s, (d) Au 4f, (e) Bi 4f, (f) S 2p in Fe_3O_4@Au@Bi_2S_3 NRs; (g) Schematic illustration of the working mechanism of Fe_3O_4@Au@Bi_2S_3 NRs in generating Vs and Bis defects to enhance photothermal performance under NIR stimulation.

into thermal energy [53]. Consequently, optimal photothermal conversion efficiency can be achieved through the strategic introduction of an adequate defect concentration.

The surface modification with PVP was further characterized using FT-IR and contact angle measurements, as shown in Fig. S3. For pure PVP, five main characteristic peaks were observed, corresponding to the stretching vibration of the O-H group, the stretching and deformation vibrations of the C-H bond, the stretching vibration of C=O, the bending vibration of C-H, and the stretching vibration of the C-N bond, respectively [54,55]. As shown in Fig. S3a, these five peaks also appeared in the FT-IR spectrum of Fe_3O_4@Au@Bi_2S_3/PVP NRs, while they were absent in the spectrum of Fe_3O_4@Au@Bi_2S_3 NRs, confirming the successful modification with PVP. Additionally, contact angle measurements were performed to assess the improvement in hydrophilicity after

PVP surface functionalization. As shown in Fig. S3b, the PVP modification significantly reduced the contact angle from ~71.9° to 29.1°, indicating a marked increase in hydrophilicity. This enhanced hydrophilicity makes Fe_3O_4@Au@Bi_2S_3/PVP NRs highly suitable for subsequent biomedical applications.

2.2. Photothermal properties

The Fe_3O_4@Au@Bi_2S_3 NRs were specifically designed to function as efficient photo-absorbers in the NIR region for PTT targeting tumor cells, necessitating a thorough evaluation of their photothermal properties (Fig. 3a–d). As shown in Fig. 3b and d, the photothermal effect of Fe_3O_4@Au@Bi_2S_3 NRs was tested under 808 nm NIR laser irradiation, with varying power densities from 0.80 to 3.40 W/cm^2. The temperature of the Fe_3O_4@Au@Bi_2S_3 NRs aqueous solution increased dramatically from 23.92 °C to 80.0 °C after 5 min of irradiation at 3.40 W/cm^2. Even at a reduced power density of 0.80 W/cm^2, the solution temperature still reached 42.05 °C, which is sufficient to induce cancer cell death.

Under a constant power density of 3.40 W/cm^2, the photothermal conversion performance of Fe_3O_4@Au@Bi_2S_3 NRs was evaluated by varying their concentration from 0 to 200 ppm (Fig. 3a and c). The results revealed a concentration-dependent increase in temperature, demonstrating that higher concentrations of Fe_3O_4@Au@Bi_2S_3 NRs resulted in a more significant temperature rise. In contrast, distilled water exhibited negligible heating under the same conditions, further confirming the concentration-dependent PCE of Fe_3O_4@Au@Bi_2S_3 NRs.

Importantly, the Fe_3O_4@Au@Bi_2S_3 NRs demonstrated remarkable photothermal stability, as no significant decrease in photothermal conversion was observed after six cycles of NIR irradiation, highlighting their durability as photothermal agents for cancer therapy (Fig. 3f). Based on the heating and cooling data in Fig. 3e, the PCE was calculated to be 44.34 %, which surpasses many previously reported materials (Table S2).

The superior PCE can be attributed to the unique core-shell structure, where the Au nanoshell serves as a receptor, closely binding with the outer Bi_2S_3 layer. The strong interaction between Au and S atoms from Bi_2S_3 led to the spoliatory loss of S atoms from the Bi_2S_3 lattice, creating sulfur vacancies (Vs). Moreover, the Bi_2S_3 nanoshell was synthesized under bismuth-rich and sulfur-deficient conditions, further promoting the formation of Vs and bismuth antisite (Bis) defects, which have low defect formation energies (Vs: 0.89 eV, Bis: 1.6 eV). These deep-level defects (DLDs) facilitated phonon emission, contributing to the material's photothermal properties [56].

The photothermal effect was further enhanced by the Au-Bi_2S_3 interaction, wherein photoexcited electrons transferred from the CB of Bi_2S_3 to the Fermi level of Au (−5.1 eV), leading to the formation of more Bis defects. This interaction introduced additional electrons through the Au Fermi level, which, in synergy with the Fe_3O_4 core, further amplified the PCE. Collectively, the combination of Fe_3O_4, Au, and Bi_2S_3 resulted in a highly effective photothermal agent, with significantly better photothermal performance compared to each individual component.

2.3. DOX collaboration

DOX has been the attention of the cancer treatment field for decades [57]. Up to now, there are still a large number of studies on the application of adriamycin in tumor therapy, such as the discovery of a conjugate [58] or system that can deliver DOX [59], the fusion of DOX with liposomes [60], and the delivery of drugs using nanomaterials as carriers [5,61], which are sufficient to prove that DOX is a successful chemotherapy drug with an outstanding effect.

Here, Fe_3O_4@Au@Bi_2S_3/PVP NRs was used as a carrier to load DOX, which combined the characteristics of drugs with the properties of the material itself to kill cancer cells in multiple ways, thus achieving remarkable results. DOX can be encapsulated within Fe_3O_4@Au@Bi_2S_3/

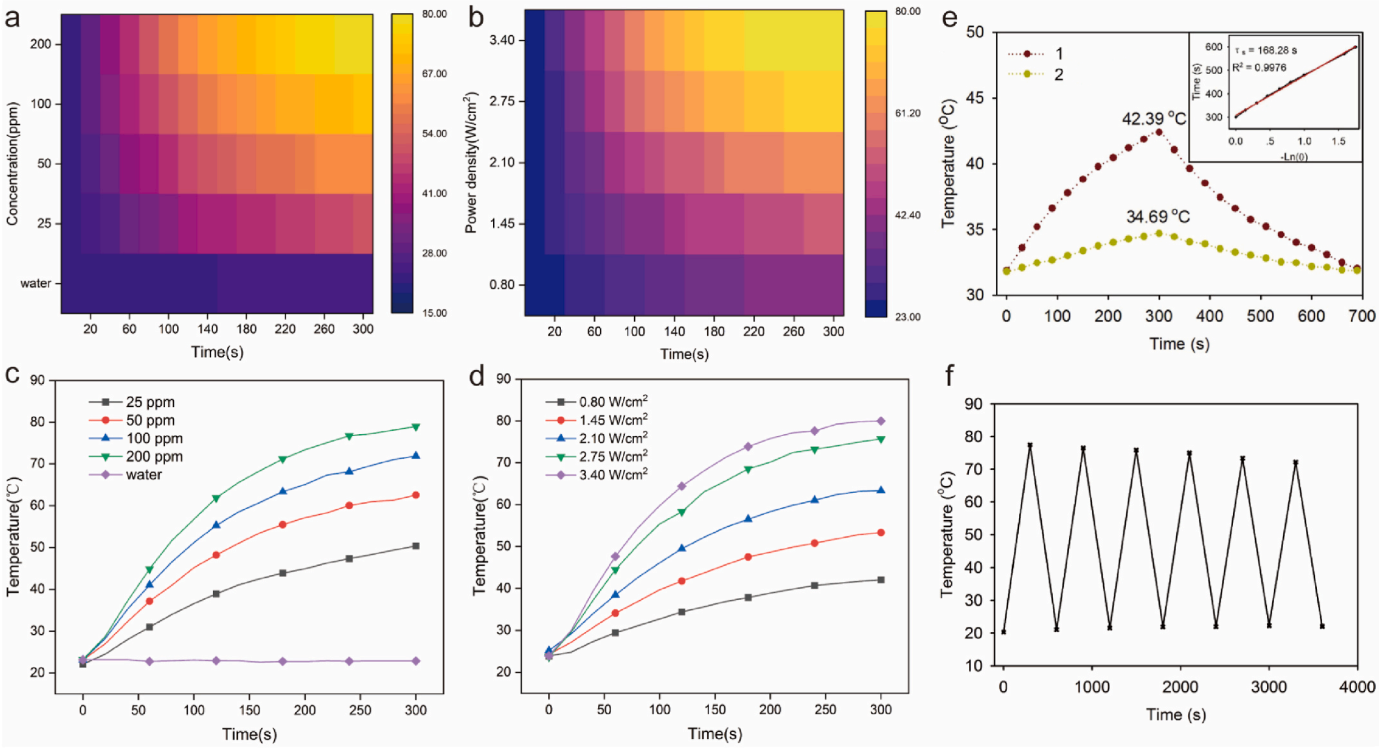

Fig. 3. Photothermal performance of Fe_3O_4@Au@Bi_2S_3 NRs: (a, c) Temperature elevation at various concentrations (0, 25, 50, 100, 200 ppm) and (b, d) under different laser power densities (0.80, 1.45, 2.10, 2.75, 3.40 W/cm^2) with 808 nm NIR irradiation for 5 min; (e) Heating and cooling curves of deionized water and Fe_3O_4@Au@Bi_2S_3 NRs dispersion (100 ppm) under 808 nm NIR irradiation (Inset: cooling time versus negative natural logarithm of the temperature-driving force); (f) Photothermal stability of Fe_3O_4@Au@Bi_2S_3 NRs dispersion (100 ppm) over 6 irradiation cycles.

PVP NRs through electrostatic interactions between DOX and PVP on the exterior of the Bi_2S_3 coating. The presence of PVP enhances the loading efficiency, facilitating pH-responsive loading and release of DOX. Studies on DOX are mainly divided into standard curve determination, load behavior and release behavior. Fig. S4a and b show the standard UV–vis absorbance curves, and the well-defined standard curve also laid a foundation for the subsequent DOX studies. The loading of DOX is mainly reflected on the change of UV–vis absorption spectra, as shown in Fig. S5. We calculated the encapsulation and loading efficiencies of DOX and compared these results with previously reported studies, demonstrating the excellent drug delivery performance of Fe_3O_4@Au@Bi_2S_3/PVP-DOX NRs (Table S3). In comparison, the curves for the composite material coated with DOX was very different from the other two curves. Also, the separation phenomenon of the material under the applied magnetic field proved that the material coated with DOX still possessed excellent magnetic properties (Fig. S4d). The premise of the killing effect of DOX on tumor cells was that the material has response effect. Therefore, it is indispensable to study the mechanism of DOX release by composite materials. PVP is amphiphilic polymer excellently sensitive to pH and thus undergoes protonation/deprotonation switch in the various pH conditions because of the existence of the hydrophilic group, tertiary amine [38]. As shown in Fig. S4c, the DOX release curve in Fe_3O_4@Au@Bi_2S_3/PVP-DOX NRs was sufficient to indicate the response of Fe_3O_4@Au@Bi_2S_3/PVP-DOX NRs to tumor cells in different pH environments. Drug release studies revealed distinct pH-dependent behavior: less than 15 % drug release within 24 h at pH 7.4, while significantly accelerated release occurred at pH 5.0. This enhanced release rate resulted from amino group protonation-induced lipophilic-to-hydrophilic transition, which generated surface channels and cracks in the polymer nanocarriers [62].

Previous studies have demonstrated that laser irradiation enhances the release rate of DOX by inducing a rapid rise in local temperature. This increase in temperature strengthens thermal vibrations and weakens the interactions between DOX and its nanoparticle carriers, thereby accelerating drug release [63]. Dou et al. designed PVP-rGO/-Bi_2S_3 nanoparticles, which exhibited a burst release of DOX under 808 nm NIR laser irradiation due to the photothermal effect. The release rate decreased once the laser was turned off [64], effectively confirming the enhanced DOX release triggered by NIR irradiation.

After successfully proving that Fe_3O_4@Au@Bi_2S_3/PVP-DOX NRs has the ability to load and release DOX, the chemotherapy effect of DOX combined with PTT and magnetic targeting of Fe_3O_4@Au@Bi_2S_3 NRs became a reality, which is another example of drug loading on nanoparticles.

2.4. *In vitro cytotoxicity and cell uptake and anti-metastasis assay*

The in vitro cytotoxicity of the Fe_3O_4@Au@Bi_2S_3/PVP-DOX NRs was evaluated using the Cell Counting Kit-8 (CCK8) assay to measure the viability of lung cancer A549 cells. The assay aimed to assess the biocompatibility and feasibility of the synthesized nanocomposites for biomedical applications (Fig. 4a). A549 cells were incubated with different concentrations of Fe_3O_4@Au@Bi_2S_3/PVP-DOX NRs for 24 h, and their viability was then measured. Additionally, the PTT potential of the Fe_3O_4@Au@Bi_2S_3/PVP-DOX NRs was examined under NIR light irradiation. As shown in Fig. 4a, cell survival rates significantly decreased upon NIR irradiation, confirming both the photothermal properties of the nanocomposites and the therapeutic efficacy of combining DOX with PTT.

DOX, a well-known chemotherapy agent, exhibits auto-fluorescence, enabling it to act as a tracer for monitoring the internalization of Fe_3O_4@Au@Bi_2S_3/PVP-DOX NRs by A549 cells. This property allowed us to investigate whether the nanoparticles were taken up by the cells via endocytosis or merely through interaction with cell surface proteins. Fluorescence images captured after 6 and 24 h of incubation revealed the uptake of Fe_3O_4@Au@Bi_2S_3/PVP-DOX NRs by A549 cells (Fig. 4c). In the presence of a magnet placed beneath the well plate, the nanoparticles accumulated locally, as demonstrated in Fig. 4b. After 6 h, red fluorescence appeared in the cytoplasm of cells incubated with Fe_3O_4@Au@Bi_2S_3/PVP-DOX NRs, indicating nanoparticle uptake. After 24 h, cells located near the magnet (Fig. 4b, Zone 2) exhibited intense red fluorescence, while cells farther from the magnet (Fig. 4b, Zone 1) showed minimal uptake. No fluorescence was observed in the control group, highlighting the successful internalization of the nanocomposites and confirming the efficacy of magnetic targeting for Fe_3O_4@Au@-Bi_2S_3/PVP-DOX NRs in the tumor microenvironment (TME).

Cancer metastasis, characterized by high cell motility and angiogenesis, presents a significant challenge in tumor eradication. To assess the anti-metastatic potential of the Fe_3O_4@Au@Bi_2S_3/PVP-DOX NRs, we performed a migration assay on A549 cells under NIR irradiation

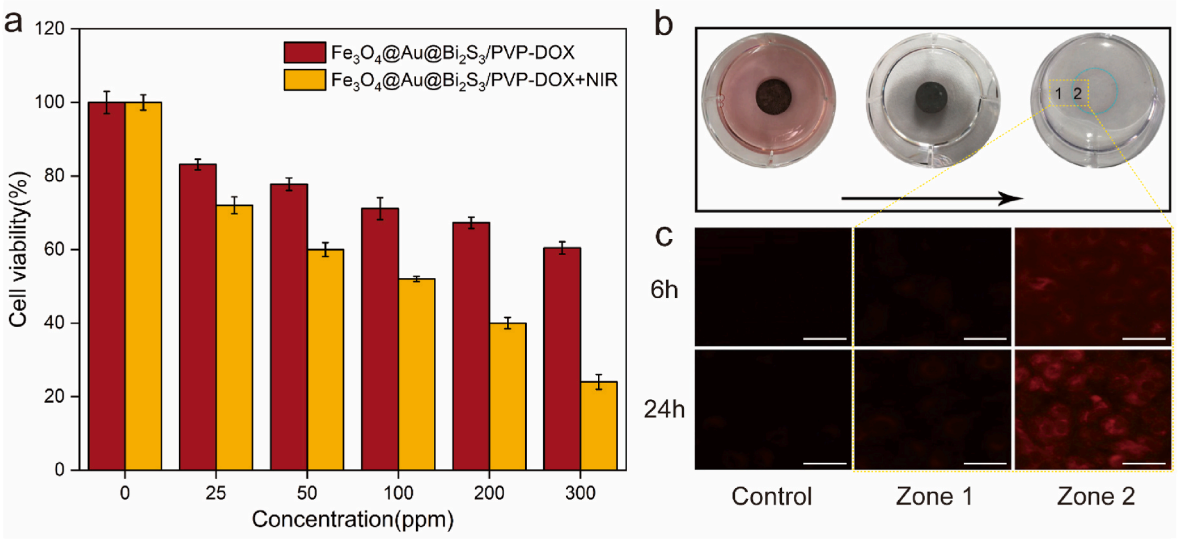

Fig. 4. a) Cell viabilities of A549 cells cultured with Fe_3O_4@Au@Bi_2S_3 NRs at various concentrations. NIR excitation power density: 1.45 W/cm^2; b) Magnetic field-mediated cell internalization experiment showing the effects of an external magnetic field on the cellular uptake of Fe_3O_4@Au@Bi_2S_3. Magnetic field strength: 0.3T; c) Fluorescence images of A549 cells corresponding to zones 1 and 2 in (b), illustrating the differential cellular internalization with and without magnetic targeting. Scale bar: 100 μm.

(Figs. S6a and b). In the control group, cancer cells exhibited a high migration rate of 72.20 %, indicating minimal inhibition of cell movement within 24 h. However, upon treatment with DOX, Fe_3O_4@Au@Bi_2S_3/PVP NRs, or Fe_3O_4@Au@Bi_2S_3/PVP-DOX NRs, the migration rates dropped to 42.66 %, 32.36 %, and 25.44 %, respectively, with Fe_3O_4@Au@Bi_2S_3/PVP-DOX NRs demonstrating the most significant inhibition of cell migration. This enhanced inhibition was attributed to the dual effects of DOX-induced cell death and the pH-responsive release of DOX from the nanoparticles, synergistically improving the therapeutic efficiency of chemo-photothermal therapy. The observed reduction in cell migration further validated the combined effects of PTT and chemotherapy.

Additionally, the colony formation assay was conducted to assess the ability of Fe_3O_4@Au@Bi_2S_3/PVP-DOX NRs to inhibit cancer cell proliferation under NIR irradiation. As shown in Figs. S6c and d, the control group exhibited substantial colony formation, while significant reductions in colony numbers were observed in the DOX and Fe_3O_4@Au@Bi_2S_3/PVP NRs groups, attributed to the therapeutic effects of either chemotherapy or PTT alone. Notably, Fe_3O_4@Au@Bi_2S_3/PVP-DOX NRs exhibited the highest inhibitory effect on A549 cell colony formation, providing strong evidence of the synergistic interaction between PTT and chemotherapy, leading to enhanced cancer cell eradication.

2.5. *In vitro cell apoptosis*

To evaluate the ability of the synthesized Fe_3O_4@Au@Bi_2S_3/PVP-DOX NRs to induce apoptosis in A549 lung cancer cells, two staining methods were employed: FITC-labeled Annexin V (Annexin V-FITC)/Propidium Iodide (PI) double staining and Hoechst 33258 staining. Both methods were used under 808 nm NIR laser exposure and an external magnetic field. The study consisted of four experimental groups: (1) control, (2) DOX, (3) Fe_3O_4@Au@Bi_2S_3/PVP NRs, and (4) Fe_3O_4@Au@Bi_2S_3/PVP-DOX NRs. Each group was subdivided into two conditions, with and without NIR irradiation. All NIR treatment groups were irradiated with 808 nm laser at 1.45 W/cm^2.

Annexin V-FITC/PI double staining: In the early stage of apoptosis, phosphatidylserine (PS) is translocated from the inner leaflet to the outer surface of the cell membrane. Annexin V-FITC binds to PS, allowing the detection of early apoptotic cells. In contrast, PI enters late apoptotic or necrotic cells, where it intercalates with DNA to emit red fluorescence. As shown in Fig. 5a, the control group exhibited almost no apoptotic cells, regardless of NIR irradiation. In the DOX group, partial apoptosis was observed, but NIR irradiation did not significantly alter the level of apoptosis. Under the condition of only Fe_3O_4@Au@Bi_2S_3/PVP NRs, compared with the control group, a small number of cancer cells underwent apoptosis, indicating that Fe_3O_4@Au@Bi_2S_3/PVP NRs have the potential to induce ferroptosis in tumor treatment (Fig. S7). The low fluorescence intensity is mainly due to the PVP modification and the multi-shell structure, which delays the induction of ferroptosis in cancer cells by Fe_3O_4@Au@Bi_2S_3/PVP NRs [65]. Fe_3O_4@Au@Bi_2S_3/PVP NRs caused more pronounced apoptosis under NIR irradiation, suggesting a photothermal effect on cancer cell treatment. Importantly, Fe_3O_4@Au@Bi_2S_3/PVP-DOX NRs exhibited a significant therapeutic

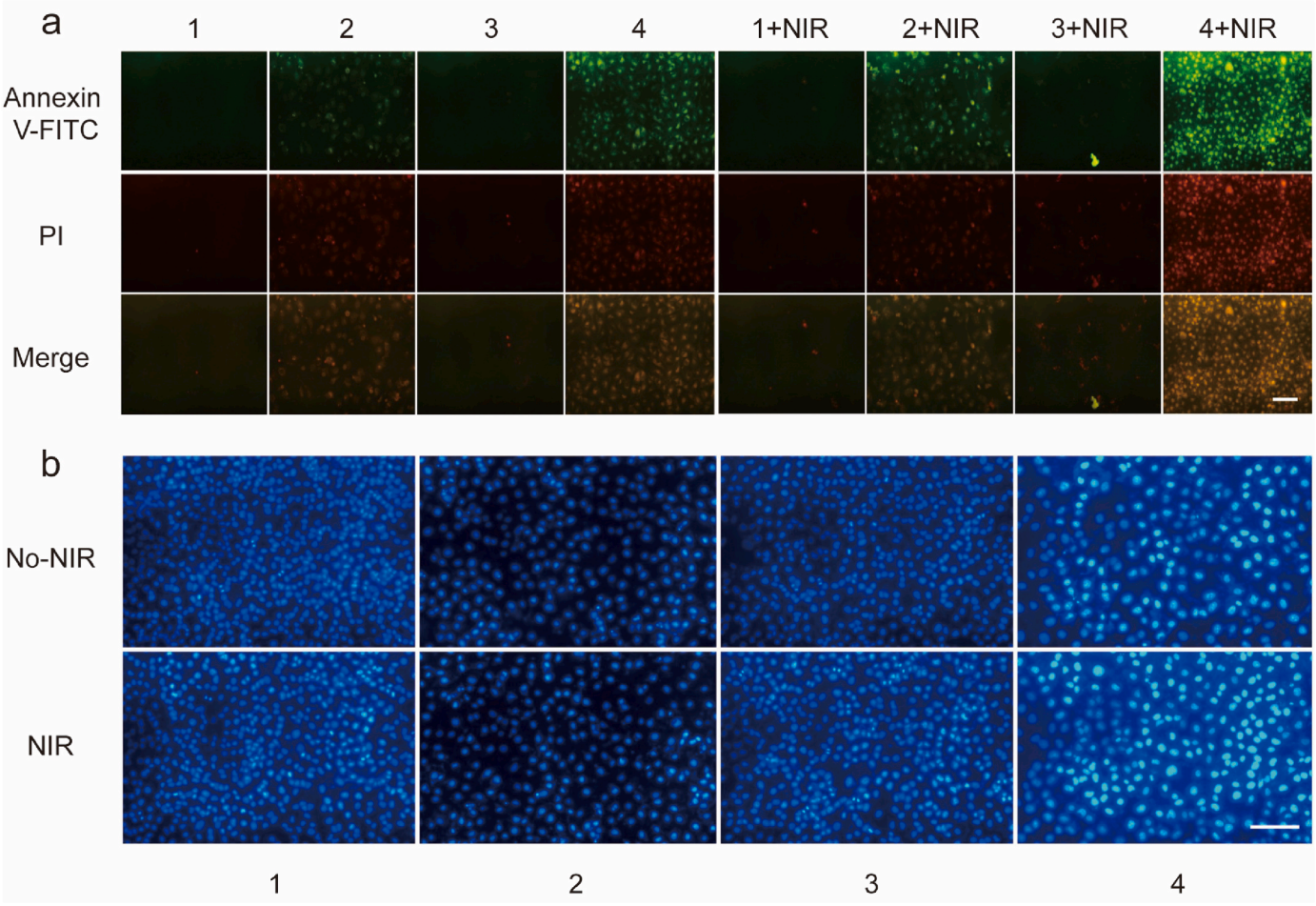

Fig. 5. (a) Annexin V-FITC/PI double staining of A549 cells, showing the apoptosis levels without and with NIR irradiation across different groups (1: Control; 2: DOX; 3: Fe_3O_4@Au@Bi_2S_3/PVP NRs; 4: Fe_3O_4@Au@Bi_2S_3/PVP-DOX NRs). Scale bar: 100 μm. (b) Hoechst 33258 staining of A549 cells, showing nuclear morphology without and with NIR irradiation across the same groups. Scale bar: 200 μm.

effect even without NIR irradiation, attributed to the release of DOX. This effect was further amplified upon NIR exposure, highlighting the synergistic effect of chemotherapy and PTT in inhibiting cancer cell proliferation.

Hoechst 33258 staining: Hoechst 33258 is a DNA-binding fluorescent dye that stains the nuclei of A549 cells blue. In apoptotic cells, chromatin condensation or fragmentation produces intense blue fluorescence, often in the form of crescent-shaped patches or fragments. In contrast, normal cells exhibit round nuclei with diffuse blue fluorescence. As seen in Fig. 5b, cells in the control group displayed normal, round-shaped nuclei with minimal signs of apoptosis, irrespective of NIR irradiation. In contrast, a significant number of apoptotic cells were observed following incubation with Fe_3O_4@Au@Bi_2S_3/PVP-DOX NRs, which increased further after 808 nm laser irradiation. Among all

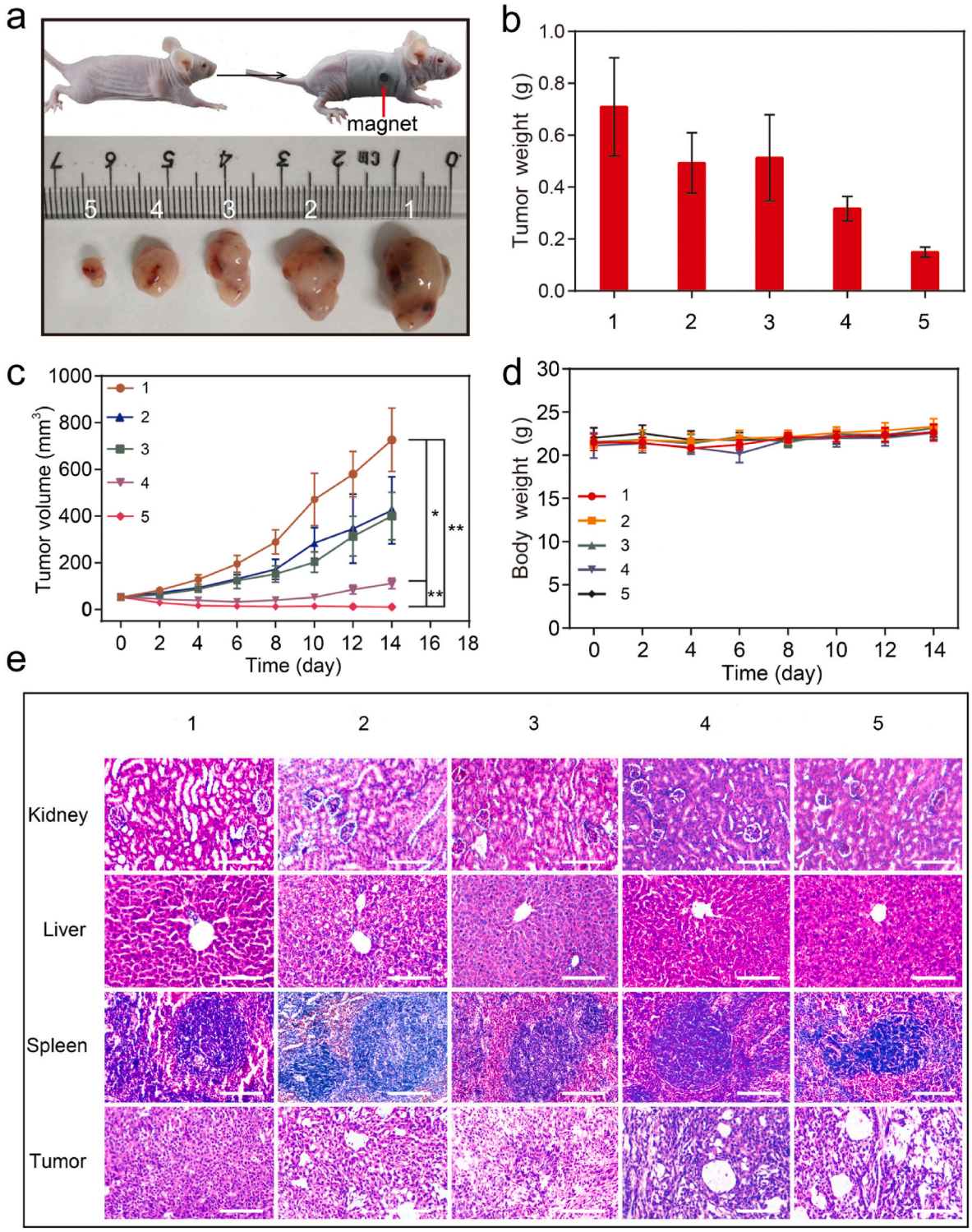

Fig. 6. a) Illustration of magnet placement on nude mice and tumor images of different treatment groups after dissection; b) Average tumor weight in each group post-dissection; c) Tumor volume progression curves during the entire treatment period; d) Body weight statistics of mice throughout the treatment; e) HE staining images of kidney, liver, spleen, and tumor tissues in each group after completing the therapy. Magnification: × 100.

groups, Fe_3O_4@Au@Bi_2S_3/PVP-DOX NRs, especially under NIR irradiation, induced the highest level of apoptosis, demonstrating the enhanced efficacy of this combination therapy.

In summary, the results of both Annexin V-FITC/PI and Hoechst 33258 staining indicate that Fe_3O_4@Au@Bi_2S_3/PVP-DOX NRs have a significantly enhanced ability to induce apoptosis in A549 cells. The combination of PTT and chemotherapy synergistically increased the therapeutic effect, leading to greater inhibition of cancer cell proliferation compared to either treatment alone. These two staining methods provided consistent and complementary evidence of the therapeutic efficacy of Fe_3O_4@Au@Bi_2S_3/PVP-DOX NRs in inducing apoptosis in A549 cells.

2.6. In vivo anti-tumor performance

A Luc-A549 tumor model was established to evaluate the NIR laser-induced therapeutic efficacy of Fe_3O_4@Au@Bi_2S_3/PVP-DOX NRs on tumor cells in vivo. A total of 25 mice were randomly divided into five groups, with each group receiving a different treatment regimen over a 14-day period (1: control; 2: DOX; 3: Fe_3O_4@ Au@Bi_2S_3/PVP; 4: Fe_3O_4@Au@Bi_2S_3/PVP-DOX + magnet; 5: Fe_3O_4@Au @Bi_2S_3/PVP-DOX + magnet + NIR; Magnetic field strength: 0.3T). Equivalent DOX doses were administered to the Fe_3O_4@ Au@Bi_2S_3/PVP-DOX + magnet + NIR group and other DOX-treated groups. Fe_3O_4@Au @Bi_2S_3/PVP-DOX + magnet + NIR group was irradiated with 808 nm laser at 1.45 W/cm^2. All mice were housed under identical growth conditions. The treatment conditions for each group are summarized in Fig. S8. Mice in all groups received either the drug or corresponding nanocomposite via tail vein injection on day 0 and day 7.

At the end of the treatment period, the tumors were excised, and their visual images are shown in Fig. 6a. The average tumor weights for each group were also recorded and compared (Fig. 6b). Tumor volumes were measured every two days throughout the study (Fig. 6c). The group treated with Fe_3O_4@Au@Bi_2S_3/PVP NRs combined with magnetic targeting (group four) demonstrated a statistically significant reduction in tumor volume compared to the control group ($P < 0.05$). Moreover, group five (Fe_3O_4@Au@Bi_2S_3/PVP-DOX NRs + NIR + magnet) showed an even more pronounced tumor volume reduction compared to the control group ($P < 0.005$), indicating the superior therapeutic efficacy of the combined PTT and chemotherapy. Importantly, group five showed the most significant reduction in tumor volume compared to group four ($P < 0.005$), highlighting the critical role of both NIR irradiation and magnetic targeting in enhancing the combined therapeutic effects of PTT and chemotherapy. This was further confirmed by the smallest tumor size and lightest tumor weight in group five, underscoring the synergistic effect of NIR irradiation and magnetic targeting in maximizing therapeutic outcomes.

The body weights of all mice were monitored throughout the treatment period, and no significant weight loss or mouse mortality was observed (Fig. 6d), indicating that Fe_3O_4@Au@Bi_2S_3/PVP-DOX NRs exhibited minimal systemic toxicity. Furthermore, tumor necrosis (blackened areas) was observed in the groups treated with DOX, Fe_3O_4@Au@Bi_2S_3/PVP-DOX NRs + magnet, and Fe_3O_4@Au@Bi_2S_3/PVP-DOX NRs + NIR + magnet, with the latter group showing the most severe necrosis, further demonstrating the efficacy of combined chemotherapy and PTT.

To confirm the safety of Fe_3O_4@Au@Bi_2S_3/PVP-DOX NRs + magnet + NIR treatment on vital organs, the livers, spleens, and kidneys were harvested at the end of the study for histological analysis using hematoxylin & eosin (HE) staining (Fig. 6e). The results showed no damage or adverse effects on the organs, with clear and intact kidney glomeruli, normal hepatocytes and central veins, and well-preserved splenic white and red pulps. This demonstrates the excellent biocompatibility and low toxicity of the Fe_3O_4@Au@Bi_2S_3/PVP NRs. Furthermore, in group five, significant cancer cell damage and irreversible necrosis were observed in the tumor tissues, while the organ tissues remained normal, further validating the safety and efficacy of the magnetic targeting Fe_3O_4@Au@Bi_2S_3/PVP NRs combined with NIR irradiation in tumor therapy.

2.7. In vivo CT imaging

In vivo fluorescence imaging provides a direct and non-invasive approach for monitoring tumor cell viability and volume in living organisms. We transfected lung cancer A549 cells with a luciferase coding gene (Luc) plasmid. The luciferase produced by these cells catalyzes the interaction between potassium luciferin and ATP, leading to the oxidation of luciferin (the substrate) and the subsequent release of photons [66]. Prior to tumor growth reaching 80 mm^3 for treatment, nude mice were anesthetized and intraperitoneally injected with potassium luciferin, followed by fluorescence imaging. As shown in Fig. 7a, at the beginning of the treatment (0th day), the tumors in all groups were of similar size. However, after 14 days of treatment, tumor sizes varied significantly among the groups due to different treatments. The control group, which received no treatment, displayed the largest tumor growth, while treatment groups showed varying degrees of tumor shrinkage. Mice treated with DOX (mouse 2), Fe_3O_4@Au@Bi_2S_3/PVP + NIR (mouse 3), Fe_3O_4@Au@Bi_2S_3/PVP-DOX + magnet (mouse 4), and Fe_3O_4@Au@Bi_2S_3/PVP-DOX + magnet + NIR (mouse 5) demonstrated reduced tumor sizes. It was concluded that magnetically targeted DOX release significantly enhanced the chemotherapy's therapeutic effect on the tumor (mouse 4), and NIR irradiation effectively triggered PTT (mouse 3). Moreover, the combination of magnetically targeted DOX release and 808 nm NIR irradiation provided the most effective tumor suppression in the Fe_3O_4@Au@Bi_2S_3/PVP-DOX NRs group (mouse 5), compared to the other groups. These fluorescence imaging results were consistent with the treatment outcomes described earlier.

Additionally, Fe_3O_4@Au@Bi_2S_3/PVP NRs demonstrated potential as a useful CT contrast agent, similar to conventional iodine-based or barium sulfate agents, due to the presence of both Au and Bi elements. As shown in Fig. 7b, enhanced brightness was observed in the tumor region after the intravenous injection of Fe_3O_4@Au@Bi_2S_3/PVP NRs, which was further intensified with the application of an external magnetic field. The CT imaging results confirmed that Fe_3O_4@Au@Bi_2S_3/PVP NRs could serve as an effective CT contrast agent, with magnetically targeted accumulation at the tumor site. Enhanced contrast signals from liver and spleen also indicated that Fe_3O_4@Au@Bi_2S_3/PVP-DOX NRs were absorbed and accumulated by the reticuloendothelial system (RES), and subsequently metabolized and cleared by liver and spleen [5].

2.8. Immunology and protein analysis

The collaborative tumor therapy model based on Fe_3O_4@Au@Bi_2S_3/PVP-DOX NRs has been validated through in vitro and in vivo experiments, demonstrating excellent anti-tumor properties. To further investigate the mechanism of tumor apoptosis induced by this therapy, we conducted detailed immunohistochemistry (IHC) and protein analysis. We divided them into 5 groups based on different treatments: 1: control, 2: DOX, 3: Fe_3O_4@Au@Bi_2S_3/PVP, 4: Fe_3O_4@Au@Bi_2S_3/PVP-DOX + magnet (0.3T), 5: Fe_3O_4@Au@Bi_2S_3/PVP-DOX + magnet (0.3T) + NIR. Equivalent DOX doses were administered to the Fe_3O_4@ Au@Bi_2S_3/PVP-DOX + magnet + NIR group and other DOX-treated groups. Fe_3O_4@Au @Bi_2S_3/PVP-DOX + magnet + NIR group was irradiated with 808 nm laser at 1.45 W/cm^2.

IHC analysis was performed to localize and quantify specific antigens within the tumor tissues. A549 tumor samples were harvested from all treatment groups after 14 days for IHC staining. The angiogenesis within tumor tissues was assessed by measuring the microvessel density through the staining of HIF-1α and CD31, both of which are indicative of tumor growth and blood vessel formation (Fig. 8a and b). The results showed that various treatments had differing levels of therapeutic

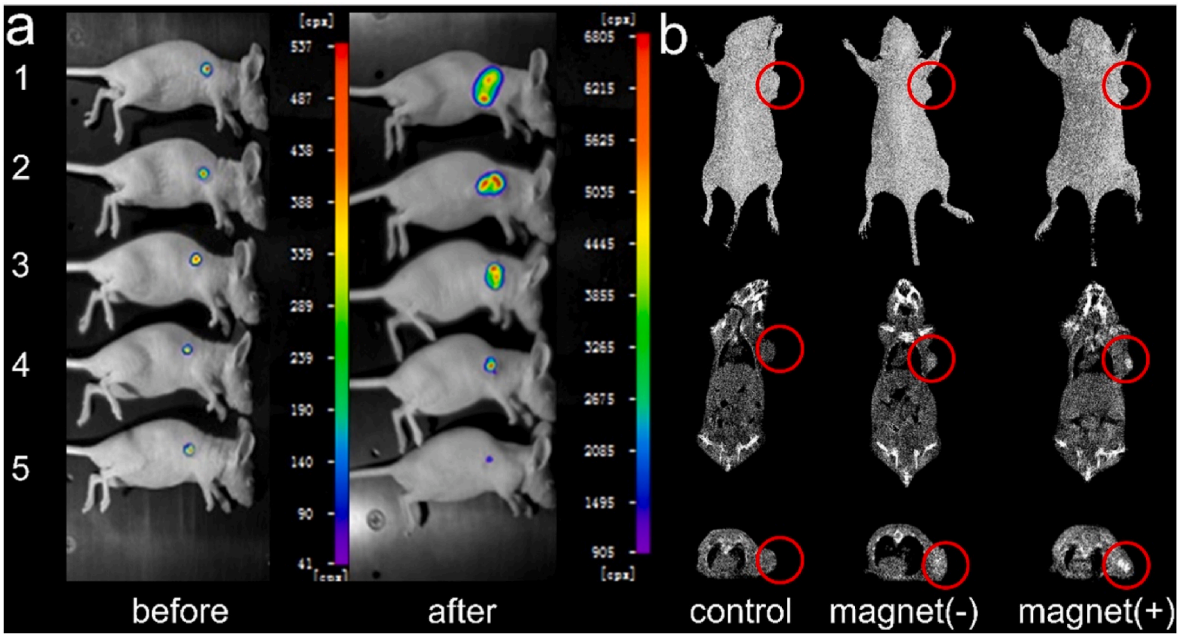

Fig. 7. a) Fluorescence imaging of tumors before and after treatment in various groups. b) CT imaging (3D imaging, platform view, and vertical section) with and without the magnet, taken 24 h after the injection of Fe_3O_4@Au@Bi_2S_3/PVP NRs. Red circles indicate the tumor positions. (1: control, 2: DOX, 3: Fe_3O_4@Au@Bi_2S_3/PVP + NIR, 4: Fe_3O_4@Au@Bi_2S_3/PVP-DOX + magnet, 5: Fe_3O_4@Au@Bi_2S_3/PVP-DOX + magnet + NIR).

effects, with the Fe_3O_4@Au@Bi_2S_3/PVP-DOX NRs combined with NIR irradiation and magnetic targeting (group 5) exhibiting the most significant inhibition of angiogenesis. The average positive staining areas for HIF-1α and CD31 were significantly lower in group 5 compared to the control group ($P < 0.01$), highlighting the effectiveness of this combination therapy in reducing tumor blood vessel formation.

In addition to angiogenesis inhibition, we examined the cell proliferation within tumor tissues using Ki-67 antibody staining. As shown in Fig. 8c and d, group 5 displayed the greatest suppression of tumor cell proliferation, with an 8-fold reduction in the Ki-67 proliferation index compared to the control group. This indicates that the combination of PTT and chemotherapy induced a strong anti-proliferative effect. Additionally, TUNEL staining was conducted to assess the extent of apoptosis within the tumor tissues. A marked increase in apoptotic cells was observed in all treatment groups, with group 5 exhibiting the highest percentage of apoptotic cells, approximately 23 % higher than the control group, further demonstrating the enhanced curative effect of Fe_3O_4@Au@Bi_2S_3/PVP-DOX NRs when combining PTT, chemotherapy, and magnetic targeting.

To further elucidate the immune response and the molecular mechanisms underlying the observed tumor inhibition, we measured intratumoral cytokine levels using the ELISA method. Key cytokines, including tumor necrosis factor-α (TNF-α), vascular endothelial growth factor (VEGF), interleukin-10 (IL-10), and transforming growth factor-β (TGF-β), were quantified (Fig. 8e). TNF-α, a pro-inflammatory cytokine that induces hemorrhagic necrosis in tumors, was significantly elevated in the collaborative treatment group, while VEGF, IL-10, and TGF-β, which promote tumor growth and immune suppression, were all down-regulated. The suppression of VEGF, a key regulator of angiogenesis, was particularly pronounced in group 5, indicating that the collaborative treatment not only inhibited tumor growth but also significantly impaired the tumor's blood supply.

To further investigate the underlying mechanisms, we analyzed the expression of key proteins involved in cell proliferation, angiogenesis, and apoptosis using western blot analysis (Fig. 8f and g). Proteins associated with tumor growth, such as HIF-1α, Cyclin D1, and VEGF, were significantly down-regulated in the group treated with Fe_3O_4@Au@Bi_2S_3/PVP-DOX + magnet + NIR. At the same time, proteins promoting apoptosis, such as Caspase-3 and Caspase-9, were upregulated. The anti-apoptotic protein Bcl-2, which is often overexpressed in cancer cells, was down-regulated in group 5, further confirming the induction of apoptosis through this treatment.

These findings align with the IHC and TUNEL results, underscoring the potential of this synergistic PTT-chemotherapy approach as an effective method for treating A549 lung cancer. The combination of photothermal therapy, chemotherapy, and magnetic targeting presents a robust strategy to inhibit tumor growth, induce apoptosis, and suppress angiogenesis, offering a promising therapeutic option for future cancer treatments.

3. Conclusions

In this study, we successfully developed a versatile rugby-like Fe_3O_4@Au@Bi_2S_3 nanoplatform with unique sulfur vacancies (Vs) and bismuth antisite (Bis) defects, designed to serve as a theranostic nanomedicine agent for magnetically targeted chemo- PTT of lung cancer, guided by enhanced CT imaging. The Fe_3O_4@Au@Bi_2S_3 NRs were synthesized under Bi-rich and S-deficient conditions, forming an ellipsoidal structure with superparamagnetic properties. The Vs and Bis defects acted as electron traps, facilitating electron-hole recombination and enhancing photothermal conversion efficiency. Despite successful enhancement of Bi_2S_3 defect density, precise defect concentration control remains a significant challenge requiring further investigation. The surface modification with PVP significantly improved the biocompatibility of the nanoplatform and allowed for pH-responsive drug loading and release, making it an effective drug carrier. Under an external magnetic field, DOX was efficiently accumulated in the tumor region and released in the acidic TME, achieving potent chemotherapy without damaging healthy tissues. The Fe_3O_4@Au@Bi_2S_3/PVP-DOX NRs also demonstrated precise tumor localization and size detection through CT imaging. Furthermore, they generated sufficient heat to induce apoptosis of cancer cells upon 808 nm NIR irradiation, enabling synergistic photothermal and chemotherapeutic effects in lung cancer treatment. The application of an external magnetic field further amplified the therapeutic efficacy by enhancing magnetic targeting.

The treatment significantly reduced tumor volumes in nude mice,

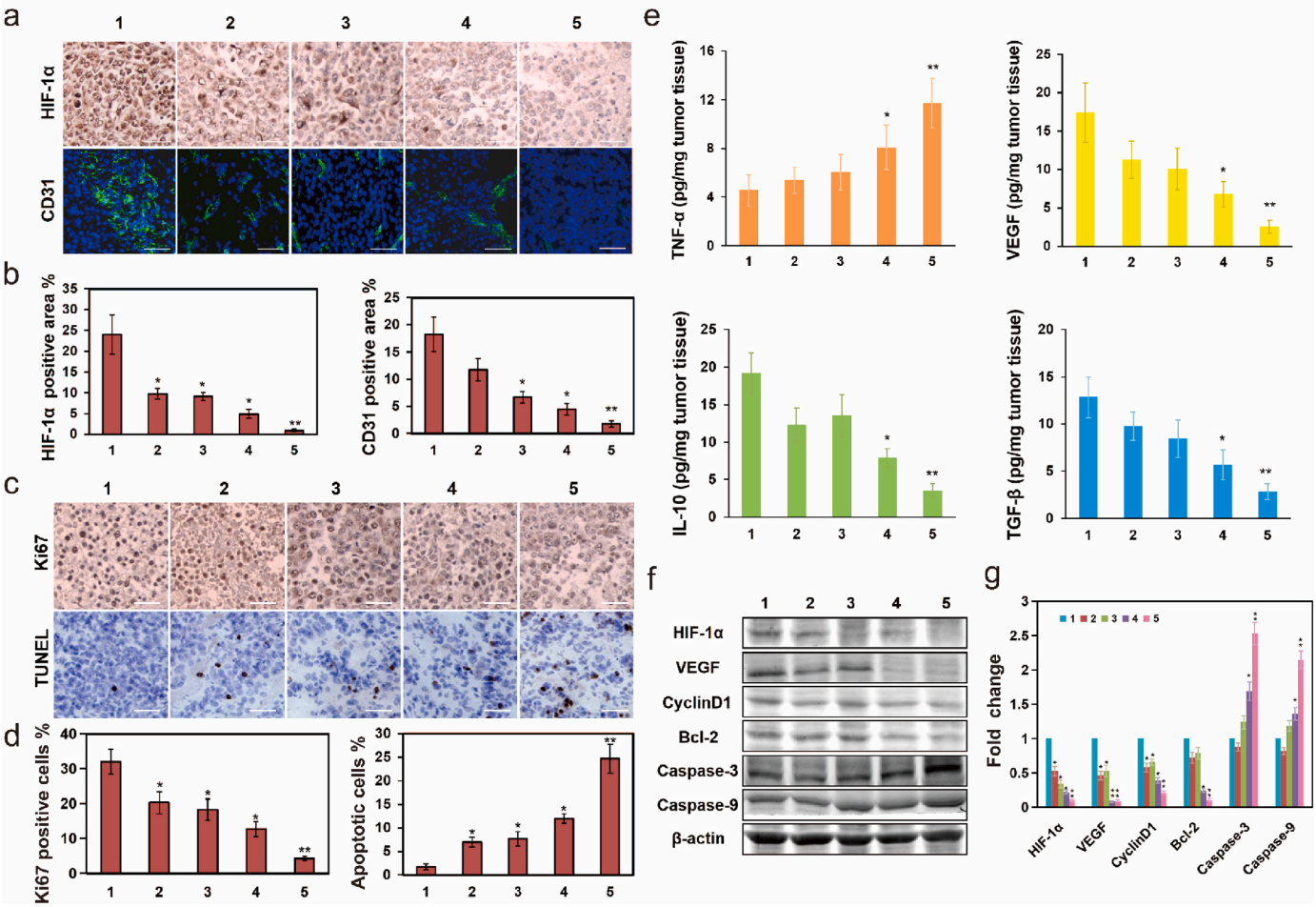

Fig. 8. Immunology and protein analysis. a) Representative images of HIF-1α positive cells and CD31 positive microvessels in tumor tissues. Scale bar: 50 μm. b) Percentage of HIF-1α positive cells and microvessel density. c) Cell proliferation indicated by Ki67 IHC staining and cell apoptosis analyzed through TUNEL staining. Scale bar: 50 μm. d) Proliferation and apoptotic indices. *P < 0.05, **P < 0.01. e) Measurement of intra-tumoral cytokine levels after collaborative treatment. *P < 0.05, **P < 0.01. f) Western blot analysis. g) Protein quantification normalized to β-actin. Data are relative to the first set (set as 1) and represent ≥2 independent experiments. *P < 0.05, **P < 0.01 vs control.

with some cases leading to complete tumor eradication, all while being closely monitored via highly contrasted CT imaging. Throughout the treatment period, no adverse effects or abnormal deaths were observed. Additionally, analysis of the tumor microenvironment confirmed that Fe_3O_4@Au@Bi_2S_3/PVP-DOX NRs effectively suppressed cancer cell proliferation and induced apoptosis, maximizing therapeutic outcomes. This study presents a promising magnetically targeted theranostic nanomedicine platform that offers enhanced efficacy for lung cancer treatment. The innovative combination of magnetic targeting, chemo-PTT, and CT imaging could provide a potent alternative for the clinical diagnosis and therapy of cancer in the near future.

CRediT authorship contribution statement

Pengpeng Jia: Writing – original draft, Validation, Methodology, Investigation, Formal analysis, Data curation, Conceptualization. **Jie Tu:** Writing – original draft, Software, Resources, Methodology, Investigation, Formal analysis, Data curation, Conceptualization. **Hongyu Shen:** Validation, Supervision, Methodology, Investigation, Data curation, Conceptualization. **Yuqin Jiang:** Validation, Methodology, Investigation, Funding acquisition. **Qiupeng Zhang:** Visualization, Software, Formal analysis. **Weixian Xue:** Validation, Software, Resources. **Meitong Liu:** Validation, Resources, Investigation. **Jianbo Liu:** Writing – review & editing, Supervision, Investigation, Conceptualization. **Yuqing Miao:** Supervision, Project administration, Funding acquisition. **Ruizhuo Ouyang:** Writing – review & editing, Supervision, Project administration, Funding acquisition, Conceptualization. **Shuang Zhou:** Supervision, Project administration, Funding acquisition, Formal analysis, Conceptualization.

Declaration of competing interest

The authors declare that they have no known competing financial interests or personal relationships that could have appeared to influence the work reported in this paper.

Acknowledgments

This work was financially supported by the Medical-Engineering Interdisciplinary Project of University of Shanghai for Science and Technology (1021341405, 1022310503), Open Research Fund of School of Chemistry and Chemical Engineering, Henan Normal University (2024Y12), the Science and Technology Project of China Minmetals Corporation (2022ZXA02), Shanghai Collaborative Innovation Center of Energy Therapy for Tumors, the Technical Innovation Team of Henan Normal University (2022TD03). The authors greatly appreciated these supports.

Appendix A. Supplementary data

Supplementary data to this article can be found online at https://doi.org/10.1016/j.mtbio.2025.101680.

Data availability

All data have been included inside the main text

References

[1] H. Sung, J. Ferlay, R.L. Siegel, M. Laversanne, I. Soerjomataram, A. Jemal, F. Bray, Global cancer statistics 2020: GLOBOCAN estimates of incidence and mortality worldwide for 36 cancers in 185 countries, CA Cancer J. Clin. 71 (3) (2021) 209–249.

[2] X. Han, J. Huang, X. Jing, D. Yang, H. Lin, Z. Wang, P. Li, Y. Chen, Oxygen-deficient black titania for synergistic/enhanced sonodynamic and photoinduced cancer therapy at near infrared-II biowindow, ACS Nano 12 (5) (2018) 4545–4555.

[3] K. Wang, Y. Xiang, W. Pan, H. Wang, N. Li, B. Tang, Dual-targeted photothermal agents for enhanced cancer therapy, Chem. Sci. 11 (31) (2020) 8055–8072.

[4] L. Li, X. Zhang, J. Zhou, L. Zhang, J. Xue, W. Tao, Non-invasive thermal therapy for tissue engineering and regenerative medicine, Small 18 (36) (2022) 2107705.

[5] R. Ouyang, P. Cao, P. Jia, H. Wang, T. Zong, C. Dai, J. Yuan, Y. Li, D. Sun, N. Guo, Bistratal Au@ Bi2S3 nanobones for excellent NIR-triggered/multimodal imaging-guided synergistic therapy for liver cancer, Bioact. Mater. 6 (2) (2021) 386–403.

[6] H. Jiang, J. Sun, F. Liu, Y. Zhao, X. Chen, C. Dai, Z. Wen, Bi2S3/Ti3C2-TPP nano-heterostructures induced by near-infrared for photodynamic therapy combined with photothermal therapy on hypoxic tumors, J. Nanobiotechnol. 22 (1) (2024) 123.

[7] Y. Li, X. Tan, H. Wang, X. Ji, Z. Fu, K. Zhang, W. Su, J. Zhang, D. Ni, Spectral computed tomography-guided photothermal therapy of osteosarcoma by bismuth sulfide nanorods, Nano Res. 16 (7) (2023) 9885–9893.

[8] J. Shan, X. Yin, S. Liu, W. Gong, Y. Bai, T. Du, J. Sun, D. Zhang, Y. Gu, J. Wang, Defect-engineering-induced vacancy-rich Bi2S3–x@ AuNPs with enhanced photothermal activity for sensitive bimodal-type gentamicin monitoring, Anal. Chem. 96 (46) (2024) 18564–18573.

[9] C. Ansari, G.A. Tikhomirov, S.H. Hong, R.A. Falconer, P.M. Loadman, J.H. Gill, R. Castaneda, F.K. Hazard, L. Tong, O.D. Lenkov, D.W. Felsher, J. Rao, H. E. Daldrup-Link, Development of novel tumor-targeted theranostic nanoparticles activated by membrane-type matrix metalloproteinases for combined cancer magnetic resonance imaging and therapy, Small 10 (3) (2014) 566–575, 417.

[10] E.A. Neuwelt, C.G. Varallyay, S. Manninger, D. Solymosi, M. Haluska, M.A. Hunt, G. Nesbit, A. Stevens, M. Jerosch-Herold, P.M. Jacobs, J.M. Hoffman, The potential of ferumoxytol nanoparticle magnetic resonance imaging, perfusion, and angiography in central nervous system malignancy: a pilot study, Neurosurgery 60 (4) (2007) 601–611. ; discussion 611-2.

[11] J. Li, B. Li, F. Liu, M. Deng, Z. Zhang, Y. Ran, B. Wang, A multifunctional nanosystem catalyzed by cascading natural glucose oxidase and Fe3O4 nanozymes for synergistic chemodynamic and photodynamic cancer therapy, Acta Biomater. 190 (2024) 518–530.

[12] Y. Zhao, J. Pan, B. Han, W. Hou, B. Li, J. Wang, G. Wang, Y. He, M. Ma, J. Zhou, Ultrahigh-resolution visualization of vascular heterogeneity in brain tumors via magnetic nanoparticles-enhanced susceptibility-weighted imaging, ACS Nano 18 (32) (2024) 21112–21124.

[13] L. Cheng, K. Yang, Y. Li, J. Chen, C. Wang, M. Shao, S.T. Lee, Z. Liu, Facile preparation of multifunctional upconversion nanoprobes for multimodal imaging and dual-targeted photothermal therapy, Angew. Chem. 50 (32) (2011) 7385–7390.

[14] M.E. Lorkowski, P.U. Atukorale, K.B. Ghaghada, E. Karathanasis, Stimuli-responsive iron oxide nanotheranostics: a versatile and powerful approach for cancer therapy, Adv. Healthcare Mater. 10 (5) (2020).

[15] S. Shen, S. Wang, R. Zheng, X. Zhu, X. Jiang, D. Fu, W. Yang, Magnetic nanoparticle clusters for photothermal therapy with near-infrared irradiation, Biomaterials 39 (2015) 67–74.

[16] S. Dutz, R. Hergt, Magnetic particle hyperthermia–a promising tumour therapy? Nanotechnology 25 (45) (2014) 452001.

[17] M. Chu, Y. Shao, J. Peng, X. Dai, H. Li, Q. Wu, D. Shi, Near-infrared laser light mediated cancer therapy by photothermal effect of Fe3O4 magnetic nanoparticles, Biomaterials 34 (16) (2013) 4078–4088.

[18] S. Zanganeh, G. Hutter, R. Spitler, O. Lenkov, M. Mahmoudi, A. Shaw, J. S. Pajarinen, H. Nejadnik, S. Goodman, M. Moseley, L.M. Coussens, H.E. Daldrup-Link, Iron oxide nanoparticles inhibit tumour growth by inducing pro-inflammatory macrophage polarization in tumour tissues, Nat. Nanotechnol. 11 (11) (2016) 986–994.

[19] R. Wei, G. Fu, Z. Li, Y. Liu, L. Qi, K. Liu, Z. Zhao, M. Xue, Au-Fe3O4 Janus nanoparticles for imaging-guided near infrared-enhanced ferroptosis therapy in triple negative breast cancer, J. Colloid Interface Sci. 663 (2024) 644–655.

[20] X. Cui, Q. Ruan, X. Zhuo, X. Xia, J. Hu, R. Fu, Y. Li, J. Wang, H. Xu, Photothermal nanomaterials: a powerful light-to-heat converter, Chem. Rev. 123 (11) (2023) 6891–6952.

[21] Y. Wang, Q. Zhang, Y. Wang, L.V. Besteiro, Y. Liu, H. Tan, Z.M. Wang, A. O. Govorov, J.Z. Zhang, J.K. Cooper, Ultrastable plasmonic Cu-based core–shell nanoparticles, Chem. Mater. 33 (2) (2020) 695–705.

[22] H. Feng, W. Wang, T. Wang, Y. Pu, C. Ma, S. Chen, Interfacial regulation of BiOI@ Bi2S3/MXene heterostructures for enhanced photothermal and photodynamic therapy in antibacterial applications, Acta Biomater. 171 (2023) 506–518.

[23] M. Zhang, Z. Xu, J. Chen, Z. Ju, Y. Ma, Z. Niu, Z. Xu, T. Zhang, F. Shi, Recent advances on nanomaterials-based photothermal sensing systems, TrAC, Trends Anal. Chem. (2024) 117801.

[24] J. Zhang, H. Chen, X. Duan, H. Sun, S. Wang, Photothermal catalysis: from fundamentals to practical applications, Mater. Today 68 (2023) 234–253.

[25] M. Ghoussoub, M. Xia, P.N. Duchesne, D. Segal, G. Ozin, Principles of photothermal gas-phase heterogeneous CO 2 catalysis, Energy Environ. Sci. 12 (4) (2019) 1122–1142.

[26] H. Jiang, X. Liu, D. Wang, Z. Qiao, D. Wang, F. Huang, H. Peng, C. Hu, Designing high-efficiency light-to-thermal conversion materials for solar desalination and photothermal catalysis, J. Energy Chem. 79 (2023) 581–600.

[27] D. Mateo, J.L. Cerrillo, S. Durini, J. Gascon, Fundamentals and applications of photo-thermal catalysis, Chem. Soc. Rev. 50 (3) (2021) 2173–2210.

[28] L.F.G. Dias, A. Abou-Hassan, Different applications, same story: inspiring nanomedicine from photothermal catalysis to modulate the photothermal activity of nanomaterials through defects engineering, Coord. Chem. Rev. 507 (2024) 215751.

[29] D. Han, M.-H. Du, C.-M. Dai, D. Sun, S. Chen, Influence of defects and dopants on the photovoltaic performance of Bi 2 S 3: first-principles insights, J. Mater. Chem. A 5 (13) (2017) 6200–6210.

[30] H.-J. Zhai, C. Bürgel, V. Bonacic-Koutecky, L.-S. Wang, Probing the electronic structure and chemical bonding of gold oxides and sulfides in AuO n− and AuS n− (n= 1, 2), J. Am. Chem. Soc. 130 (28) (2008) 9156–9167.

[31] Y. Cheng, Y. Chang, Y. Feng, H. Jian, Z. Tang, H. Zhang, Deep-level defect enhanced photothermal performance of bismuth sulfide-gold heterojunction nanorods for photothermal therapy of cancer guided by computed tomography imaging, Angew. Chem. 57 (1) (2018) 246–251.

[32] M. Jeon, G. Kim, W. Lee, S. Baek, H.N. Jung, H.-J. Im, Development of theranostic dual-layered Au-liposome for effective tumor targeting and photothermal therapy, J. Nanobiotechnol. 19 (2021) 1–16.

[33] N. Li, Y. Wang, Y. Li, C. Zhang, G. Fang, Recent advances in photothermal therapy at near-infrared-II based on 2D MXenes, Small 20 (6) (2024) 2305645.

[34] C. Ji, M. Zhao, C. Wang, R. Liu, S. Zhu, X. Dong, C. Su, Z. Gu, Biocompatible tantalum nanoparticles as radiosensitizers for enhancing therapy efficacy in primary tumor and metastatic sentinel lymph nodes, ACS Nano 16 (6) (2022) 9428–9441.

[35] P. Ghutepatil, V.M. Khot, A.B. Salunkhe, Design of monodispersed PVP functionalized biocompatible manganese ferrite nanoparticles for hyperthermia application, Mater. Today Proc. 62 (2022) 5341–5346.

[36] M. Zhang, Y. Chen, Q. Wang, C. Li, C. Yuan, J. Lu, Y. Luo, X. Liu, Nanocatalytic theranostics with intracellular mutual promotion for ferroptosis and chemo-photothermal therapy, J. Colloid Interface Sci. 657 (2024) 619–631.

[37] X. Yang, H. Zhang, Z. Wu, Q. Chen, W. Zheng, Q. Shen, Q. Wei, J.-W. Shen, Y. Guo, Tumor therapy utilizing dual-responsive nanoparticles: a multifaceted approach integrating calcium-overload and PTT/CDT/chemotherapy, J. Contr. Release 376 (2024) 646–658.

[38] J.e. Wang, G. Wang, Y. Sun, Y. Wang, Y. Yang, Y. Yuan, Y. Li, C. Liu, In Situ formation of pH-/thermo-sensitive nanohybrids via friendly-assembly of poly(N-vinylpyrrolidone) onto LAPONITE®, RSC Adv. 6 (38) (2016) 31816–31823.

[39] N. Yan, Y. Yuan, P.J. Dyson, Rhodium nanoparticle catalysts stabilized with a polymer that enhances stability without compromising activity, Chem. Commun. 47 (9) (2011) 2529–2531.

[40] S. Nigam, K.C. Barick, D. Bahadur, Development of citrate-stabilized Fe3O4 nanoparticles: conjugation and release of doxorubicin for therapeutic applications, J. Magn. Magn Mater. 323 (2) (2011) 237–243.

[41] H. Chen, F. Qi, H. Zhou, S. Jia, Y. Gao, K. Koh, Y. Yin, Fe3O4@Au nanoparticles as a means of signal enhancement in surface plasmon resonance spectroscopy for thrombin detection, Sensor. Actuator. B Chem. 212 (2015) 505–511.

[42] L. Ma, S. Liang, X.-L. Liu, D.-J. Yang, L. Zhou, Q.-Q. Wang, Synthesis of dumbbell-like gold-metal sulfide core-shell nanorods with largely enhanced transverse plasmon resonance in visible region and efficiently improved photocatalytic activity, Adv. Funct. Mater. 25 (6) (2015) 898–904.

[43] W.P. Li, P.Y. Liao, C.H. Su, C.S. Yeh, Formation of oligonucleotide-gated silica shell-coated Fe(3)O(4)-Au core-shell nanotrisoctahedra for magnetically targeted and near-infrared light-responsive theranostic platform, J. Am. Chem. Soc. 136 (28) (2014) 10062–10075.

[44] X. Ji, X. Song, J. Li, Y. Bai, W. Yang, X. Peng, Size control of gold nanocrystals in citrate reduction: the third role of citrate, J. Am. Chem. Soc. 129 (45) (2007) 13939–13948.

[45] D.A. Zweifel, A. Wei, Sulfide-arrested growth of gold nanorods, Chem. Mater. 17 (16) (2005) 4256–4261.

[46] Y. Yang, M. Sun, Z. Chen, H. Xu, X. Wang, J. Duan, B. Hou, 3D nanothorn cluster-like Zn-Bi2S3 sensitized WO3/ZnO multijunction with electron-storage characteristic and adjustable energy band for improving sustained photoinduced cathodic protection application, Chem. Eng. J. 458 (2023) 141458.

[47] W. Shangguan, Q. Liu, Y. Wang, N. Sun, Y. Liu, R. Zhao, Y. Li, C. Wang, J. Zhao, Molecular-level insight into photocatalytic CO2 reduction with H2O over Au nanoparticles by interband transitions, Nat. Commun. 13 (1) (2022) 3894.

[48] Y. Yang, K. Jiang, J. Guo, J. Li, X. Peng, B. Hong, X. Wang, H. Ge, Facile fabrication of Au/Fe3O4 nanocomposites as excellent nanocatalyst for ultrafast recyclable reduction of 4-nitropheol, Chem. Eng. J. 381 (2020) 122596.

[49] X. Wang, C. Zhang, J. Du, X. Dong, S. Jian, L. Yan, Z. Gu, Y. Zhao, Enhanced generation of non-oxygen dependent free radicals by Schottky-type

heterostructures of Au–Bi2S3 nanoparticles via X-ray-induced catalytic reaction for radiosensitization, ACS Nano 13 (5) (2019) 5947–5958.
[50] J. Grigas, E. Talik, V. Lazauskas, X-ray photoelectron spectra and electronic structure of Bi2S3 crystals, Phys. Status Solidi 232 (2) (2002) 220–230.
[51] H. Wang, L. Wang, D. Lin, X. Feng, Y. Niu, B. Zhang, F.-S. Xiao, Strong metal–support interactions on gold nanoparticle catalysts achieved through Le Chatelier's principle, Nat. Catal. 4 (5) (2021) 418–424.
[52] Z. Shao, H. Meng, J. Sun, N. Guo, H. Xue, K. Huang, F. He, F. Li, Q. Wang, Engineering of amorphous structures and sulfur defects into ultrathin FeS nanosheets to achieve superior electrocatalytic alkaline oxygen evolution, ACS Appl. Mater. Interfaces 12 (46) (2020) 51846–51853.
[53] S. Zhu, S. Xu, Y. Guo, H. Zhang, K. Ma, J. Wang, Q. Zhao, L. Zhou, W. Cai, Defect damping-enhanced plasmonic photothermal conversion, ACS Nano 17 (11) (2023) 10300–10312.
[54] X. Sui, Y. Liu, C. Shao, Y. Liu, C. Xu, Structural and photoluminescent properties of ZnO hexagonal nanoprisms synthesized by microemulsion with polyvinyl pyrrolidone served as surfactant and passivant, Chem. Phys. Lett. 424 (4–6) (2006) 340–344.
[55] S. Wang, J. Zhao, H. Yang, C. Wu, F. Hu, H. Chang, G. Li, D. Ma, D. Zou, M. Huang, Bottom-up synthesis of WS2 nanosheets with synchronous surface modification for imaging guided tumor regression, Acta Biomater. 58 (2017) 442–454.
[56] R.Z. Ouyang, Y. Yang, X. Tong, K. Feng, Y.Q. Yang, H.H. Tao, X.S. Zhang, T. Y. Zong, P.H. Cao, F. Xiong, N. Guo, Y.H. Li, Y.Q. Miao, S. Zhou, Potent anticancer activity of a new bismuth (III) complex against human lung cancer cells, J. Inorg. Biochem. 168 (2017) 18–26.
[57] K. Yoshikawa, H. Kitaoka, Prolonged intra-aortic infusion therapy with anti-tumor agents for advanced cancer of the stomach, colon and rectum, Jpn. J. Surg. 1 (4) (1971) 256–262.
[58] S. Cai, S. Thati, T.R. Bagby, H.-M. Diab, N.M. Davies, M.S. Cohen, M.L. Forrest, Localized doxorubicin chemotherapy with a biopolymeric nanocarrier improves survival and reduces toxicity in xenografts of human breast cancer, J. Contr. Release 146 (2) (2010) 212–218.
[59] L. Dong, S. Xia, K. Wu, Z. Huang, H. Chen, J. Chen, J. Zhang, A pH/Enzyme-responsive tumor-specific delivery system for doxorubicin, Biomaterials 31 (24) (2010) 6309–6316.
[60] K.-i. Ogawara, K. Un, K.-i. Tanaka, K. Higaki, T. Kimura, In vivo anti-tumor effect of PEG liposomal doxorubicin (DOX) in DOX-resistant tumor-bearing mice: involvement of cytotoxic effect on vascular endothelial cells, J. Contr. Release 133 (1) (2009) 4–10.
[61] R. Han, Q. Liu, Y. Lu, J. Peng, M. Pan, G. Wang, W. Chen, Y. Xiao, C. Yang, Z. Qian, Tumor microenvironment-responsive Ag2S-PAsp(DOX)-cRGD nanoparticles-mediated photochemotherapy enhances the immune response to tumor therapy, Biomaterials 281 (2022) 121328.
[62] M. Kanamala, W.R. Wilson, M. Yang, B.D. Palmer, Z. Wu, Mechanisms and biomaterials in pH-responsive tumour targeted drug delivery: a review, Biomaterials 85 (2016) 152–167.
[63] Y. Huang, Z. Xue, S. Zeng, Hollow mesoporous Bi@ PEG-FA nanoshell as a novel dual-stimuli-responsive nanocarrier for synergistic chemo-photothermal cancer therapy, ACS Appl. Mater. Interfaces 12 (28) (2020) 31172–31181.
[64] R. Dou, Z. Du, T. Bao, X. Dong, X. Zheng, M. Yu, W. Yin, B. Dong, L. Yan, Z. Gu, The polyvinylpyrrolidone functionalized rGO/Bi 2 S 3 nanocomposite as a near-infrared light-responsive nanovehicle for chemo-photothermal therapy of cancer, Nanoscale 8 (22) (2016) 11531–11542.
[65] A. Fromain, J.E. Perez, A. Van de Walle, Y. Lalatonne, C. Wilhelm, Photothermia at the nanoscale induces ferroptosis via nanoparticle degradation, Nat. Commun. 14 (1) (2023) 4637.
[66] A.J. Syed, J.C. Anderson, Applications of bioluminescence in biotechnology and beyond, Chem. Soc. Rev. 50 (9) (2021) 5668–5705.